Quantum effects in the structural and elastic properties of graphite: Path-integral simulations

Carlos P. Herrero ●* and Rafael Ramírez ●

*Instituto de Ciencia de Materiales de Madrid, Consejo Superior de Investigaciones Científicas (CSIC),
Campus de Cantoblanco, 28049 Madrid, Spain*

Graphite, as a well-known carbon-based solid, is a paradigmatic example of the so-called van der Waals layered materials, which display a large anisotropy in their physical properties. Here we study quantum effects in structural and elastic properties of graphite by using path-integral molecular dynamics simulations in the temperature range from 50 to 1500 K. This method takes into account quantization and anharmonicity of vibrational modes in the material. Our results are compared with those found by using classical molecular dynamics simulations. We analyze the volume and in-plane area as functions of temperature and external stress. The quantum motion is essential to correctly describe the in-plane and out-of-plane thermal expansion. Quantum effects cause also changes in the elastic properties of graphite with respect to a classical model. At low temperature we find an appreciable decrease in the linear elastic constants, mainly in C_{12} and C_{44}. Quantum corrections in stiffness constants can be in some cases even larger than 20%. The bulk modulus and Poisson's ratio are reduced by 4% and 19%, respectively, due to zero-point motion of the C atoms. These quantum effects in structural and elastic properties of graphite are non-negligible up to temperatures higher than 300 K.

I. INTRODUCTION

Over the last few decades, we have witnessed much progress in the knowledge of carbon-based materials with sp^2 orbital hybridization, such as fullerenes, carbon nanotubes, and graphene [1–4], which has progressively broadened the scope of this research field further than the traditionally known graphite. This classical material has in turn become a paradigmatic case of the nowadays called van der Waals materials, characterized by a layered structure, where the interactions between sheets are much weaker than those between atoms in each sheet [5]. Among these materials one finds hexagonal boron nitride, transition-metal dichalcogenides, and III-VI compounds such as InSe and GaS [6].

In addition to its common role in several areas such as lubrication, batteries, and nuclear technology, graphite has had a renewed interest in recent years in connection with the discovery of graphene and the potential applications of this two-dimensional material. In particular, mechanical properties of graphite, including elastic constants, have been studied by using experimental and theoretical methods [7–15]. Nevertheless, a precise knowledge of these properties has been limited by the difficulty of obtaining high-quality single-crystalline samples [16,17]. Thus, although there is a general agreement on the values of the largest elastic stiffness constants (i.e., their relative uncertainty is a few percent), values of smaller elastic constants such as C_{44} and C_{13} are known with relatively large error bars. For C_{13}, for example, one finds in the literature values of 0(3) GPa [8] and 15(5) GPa

[7], derived from apparently reliable methods. This is in part due to the high anisotropy of graphite, which means that elastic stiffness constants related to in-plane deformations, such as C_{11} and C_{12}, are much larger than those related to deformations along the z axis perpendicular to the basal plane.

Theoretical work has been carried out to study structural, elastic, and thermodynamic properties of graphite. Most of the calculations and simulations performed to analyze such properties of graphite (and solids in general) have considered atomic nuclei as classical particles. This means that their quantum zero-point motion is not taken into account in zero-temperature calculations, and their motion is assumed to be classical (i.e., follows Newton's laws) in finite-temperature Monte Carlo or molecular dynamics (MD) simulations. The quantum delocalization of atomic nuclei becomes unimportant at high temperatures, but can lead to appreciable corrections in physical observables for T lower than the Debye temperature of the material, Θ_D [18]. Throughout this paper we call nuclear quantum effects those caused by the quantum nature of atomic nuclei, which manifests itself in a spatial delocalization larger than that expected for a classical calculation (thermal motion).

Several research groups employed density-functional theory (DFT) calculations at $T = 0$, and in some cases finite temperatures were considered by using a quantum quasi-harmonic approximation (QHA) for the vibrational modes [13,19,20]. This approach is generally accepted to be sound at low temperature, but it can be inaccurate for layered materials at relatively high temperatures, as a consequence of an appreciable anharmonic coupling between out-of-plane and in-plane vibrational modes, which is not considered in a QHA. Various works based on classical molecular dynamics and

*ch@icmm.csic.es

Monte Carlo simulations of graphite have also appeared in the literature [21–27]. For this layered material, frequencies of out-of-plane vibrational modes are lower than those of in-plane vibrations, and one can define two different Debye temperatures, one for the first set of modes ($\Theta_D^{out} \sim 1000$ K) and another for the second ($\Theta_D^{in} \sim 2500$ K) [28,29]. This means that nuclear quantum effects are expected to be appreciable at temperatures on the order of 300 K and even higher.

The difficulties associated with using classical simulations can be surmounted by employing simulation techniques which take account of nuclear quantum effects in an explicit way, such as those based on Feynman path integrals [30–33]. This procedure is in principle equivalent to a quantization of the vibrational modes in the solid, with the advantage that anharmonicities are directly included in the path-integral simulation procedures. These kinds of methods have been used to study properties of materials such as diamond [34,35], silicon [36], boron nitride [37,38], and graphene [32,33,39]. We are not aware of any quantum atomistic simulation of graphite. An important point is the large anisotropy of this material, so that quantum effects can be quantitatively very different for properties along directions on the basal plane or perpendicular to it.

Here we employ the path-integral molecular dynamics (PIMD) method to study structural and elastic properties of graphite in a temperature range from 50 to 1500 K. The importance of nuclear quantum effects in the considered variables is assessed by comparing the results of quantum simulations with those obtained from classical MD simulations. We find that considering nuclear quantum motion is necessary for an adequate description of the in-plane thermal expansion. In general, quantum effects are non-negligible in structural and elastic properties of graphite for temperatures even higher than 300 K. Particular attention is set on the temperature dependence of the linear elastic constants and bulk modulus of graphite. At low temperature, quantum corrections in elastic stiffness constants may be higher than 20%, whereas the Poisson's ratio and bulk modulus are appreciably reduced.

The paper is organized as follows. In Sec. II we describe the computational methods employed in the simulations. In Sec. III we discuss the phonon dispersion bands and the calculation of elastic constants at $T = 0$. Results for the internal energy of graphite are presented in Sec. IV. In Sec. V we show results for the volume and the in-plane area, and the thermal expansion is presented in Sec. VI. Data of the elastic constants and bulk modulus at finite temperatures are given and discussed in Secs. VII and VIII. Finally, we summarize the main results in Sec. IX.

II. COMPUTATIONAL METHOD

In this paper we study the influence of nuclear quantum effects on structural and elastic properties of graphite. This means that we consider quantum delocalization of atomic nuclei, and analyze its influence on physical observables of the material. This requires, on one side, the definition of a reliable potential to describe the interatomic interactions in the solid. This potential is usually derived from *ab initio* methods (e.g., DFT), tight-binding-like Hamiltonians, or effective interactions. This provides one with a Born-Oppenheimer surface

for motion of the atomic nuclei. On the other side, we need a method to take into account the quantum dynamics (or quantum delocalization) in the many-body configuration space of atomic coordinates with the selected interatomic interactions. This means that we have to base our finite-temperature calculations on quantum statistical physics, in contrast to the more usually employed classical statistical physics to perform Monte Carlo or molecular dynamics simulations.

Thus, we employ PIMD simulations to study equilibrium properties of graphite as a function of temperature and pressure. The PIMD method rests on the Feynman path-integral formulation of statistical mechanics [40], which turns out to be a suitable nonperturbative procedure to study many-body quantum systems at finite temperatures. In the implementation of this method, each quantum particle (here, atomic nucleus) is described as a set of N_{Tr} (Trotter number) beads, which act as classical particles building a ring polymer [30,31]. In this way, one has a *classical isomorph* displaying an unreal dynamics, as it does not represent the true dynamics of the actual quantum particles. This isomorph is, however, practical for an efficient sampling of the configuration space, thus giving accurate values for time-independent variables of the quantum system. Details on this simulation technique can be found in Refs. [30,31,41,42].

Interatomic interactions between C atoms are described here through a long-range bond order potential, the so-called LCBOPII, mainly employed earlier to perform classical simulations of carbon-based systems [43]. Notably, it has been used to study the phase diagram of carbon, including graphite, diamond, and the liquid, and displayed its precision by yielding rather accurately the graphite-diamond transition line [21]. More recently, this effective potential has been also found to accurately describe various properties of graphene [44–48].

The LCBOPII potential was also employed in the last years to perform PIMD simulations, providing a quantification of nuclear quantum effects in monolayer and bilayer graphene from a comparison with results of classical simulations [33,49]. In this paper about graphite, as in earlier simulations of graphene [33,48,50], the original parametrization of the LCBOPII potential has been slightly modified to increase the zero-temperature bending constant κ of the graphene layers from 1.1 eV to 1.49 eV, closer to experimental data [51,52]. The interlayer interaction was fitted to the results of quantum Monte Carlo calculations [53], to yield a binding energy of 50 meV/atom for graphite [54].

For the calculations presented here, we have employed both the isothermal-isobaric (NPT) and isothermal-isochoric (NVT) ensembles. For the NVT simulations we used cell parameters obtained from equilibrium NPT simulations at the same temperature. We have used effective algorithms for the PIMD simulations, such as those presented in the literature [55–57]. In particular, we have employed staging coordinates to define the bead positions in the classical isomorph, and in order to keep a constant T we have introduced chains of four Nosé-Hoover thermostats connected to each staging coordinate. In NPT simulations, another chain of four thermostats was coupled to the barostat to give the equilibrium volume fluctuations for the considered external stress [41,58]. The equations of motion have been integrated by using the
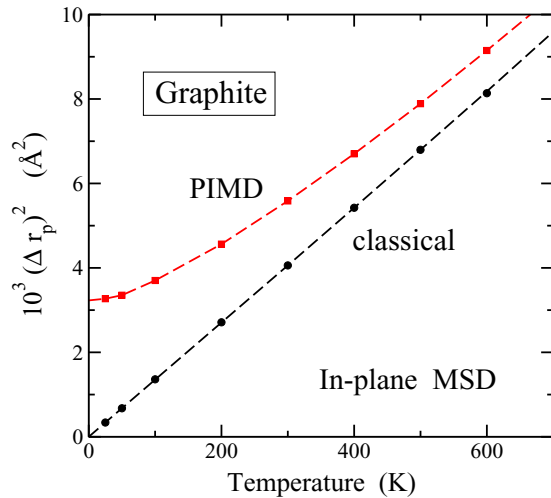
FIG. 1. In-plane mean-square displacement, $(\Delta r_p)^2 = (\Delta x)^2 + (\Delta y)^2$, of carbon atoms in graphite, as derived from classical MD (circles) and quantum PIMD simulations (squares) at various temperatures. Error bars are less than the symbol size.

reversible reference system propagator algorithm (RESPA), which allows us to consider different time steps for the integration of the slow and fast degrees of freedom [59]. The time step corresponding to the interatomic forces was $\Delta t = 1$ fs, which is adequate for the C atomic mass and the range of temperatures considered here. More details on this type of PIMD simulations are given elsewhere [56,60,61].

We considered orthorhombic simulation cells of graphite with $N = 960$ atoms and similar side lengths in the in-plane x and y directions ($L_x \approx L_y$). These cells included four carbon sheets in AB stacking, each with $n = 240$ atoms. Periodic boundary conditions were assumed. To check the convergence of our results, some simulations were carried out for larger simulation cells with $n = 960$ atoms. As the size n is increased, there appear vibrational modes with longer wavelength λ. In fact, one has an effective wavelength cutoff $\lambda_{\max} \approx L$, where $L = (L_x L_y)^{1/2}$, which translates into a wave vector cutoff $k_{\min} \approx 2\pi/L$, with $k = |\mathbf{k}|$. The results obtained using $n = 240$ and 960 atoms/layer for the energy, in-plane area, and interatomic distances coincide within the statistical error bars of our simulations. For example, for the energy and mean interatomic distance, differences are less than 6×10^{-4} eV/atom and 4×10^{-5} Å, respectively.

Sampling of the configuration space was performed in the temperature range between 50 K and 1500 K. The Trotter number N_{Tr} (number of beads in the ring polymers) varies with the temperature as $N_{\mathrm{Tr}} = 6000$ K$/T$, which gives a roughly constant accuracy of the PIMD results for different temperatures [60–62]. A typical simulation run in the NVT or NPT ensembles consisted of 2×10^5 PIMD steps for system equilibration and 8×10^6 steps for calculation of average variables. For comparison with the results of our quantum PIMD simulations, we have also carried out classical molecular dynamics simulations with the same interatomic potential. In our context, these classical simulations correspond to a Trotter number $N_{\mathrm{Tr}} = 1$.

In Fig. 1 we present the mean-square displacement (MSD) of carbon atoms in the (x, y) layer plane, $(\Delta r_p)^2 = (\Delta x)^2 + (\Delta y)^2$, at several temperatures and zero external pressure. Solid circles represent data points obtained from classical MD simulations, whereas squares indicate results of PIMD simulations. The classical results converge to zero in the low-temperature limit, as expected in classical physics, while the quantum data converge at low T to $(\Delta r_p)^2 = 3.4 \times 10^{-3}$ Å^2 (in-plane zero-point delocalization). The difference between classical and quantum results decreases as temperature is raised, but is clearly appreciable in the whole temperature range displayed in Fig. 1. An even larger quantum delocalization occurs for the out-of-plane z direction, which has been studied in detail for graphene in Ref. [33]. Such atomic quantum delocalization (in-plane and out-of-plane) causes changes in the properties of the material, especially in the presence of anharmonicities in the lattice vibrations, as the atomic motion "explores" larger regions of the configuration space, as compared to classical simulations.

The elastic stiffness constants at $T = 0$ have been calculated from the phonon dispersion bands and cell distortions as explained in Sec. III. Relations between the elastic stiffness constants C_{ij} and compliance constants S_{ij} for hexagonal crystals, as well as their definitions as functions of the strain and stress components, e_{ij} and τ_{ij}, are given in the literature [63–65]. We use the standard notation for strain components, with $e_{ij} = \epsilon_{ij}$ for $i = j$, and $e_{ij} = 2\epsilon_{ij}$ for $i \neq j$ [63,66].

At finite temperatures, we have also obtained the elastic constants of graphite in two different ways. The first way consists of applying a certain component of the stress tensor in isothermal-isobaric simulations, and obtaining the associated elastic constants from the resulting strain. Thus, for example, for $\tau_{xx} \neq 0$ and $\tau_{ij} = 0$ for the other components we can calculate S_{11}, S_{12}, and S_{13}. Then, from the obtained compliance constants we calculate the stiffness constants C_{ij} using the relations corresponding to hexagonal crystals [63–65].

In the second way, we take as a reference for each temperature and kind of simulation (classical MD or PIMD) the simulation cell parameters obtained from equilibrium isothermal-isobaric simulations at that temperature. Then, we carry out NVT simulations for cells strained a certain amount with respect the equilibrium one. For example, for $e_{zz} \neq 0$ and $e_{ij} = 0$ for the other components of the strain tensor, we obtain a stress tensor $\{\tau_{ij}\}$ from which we calculate the stiffness constants C_{13} and C_{33}. Comparing the results of both methods provides us with a consistency check for our calculations.

III. PHONON DISPERSION BANDS AND ELASTIC CONSTANTS AT $T = 0$

The evaluation of the elastic stiffness constants, C_{ij}, of graphite with the LCBOPII potential model in the classical $T \to 0$ limit provides us with a useful reference for the subsequent analysis of temperature and nuclear quantum effects. Two alternative methods have been employed to derive C_{ij} in this limit, namely the analysis of the harmonic dispersion relation of acoustic phonons, and the calculation of the elastic energy associated with some selected strain tensors, $\{e_{ij}\}$.

The phonon bands of graphite derived from the LCBOPII potential employed here are displayed in Fig. 2. These
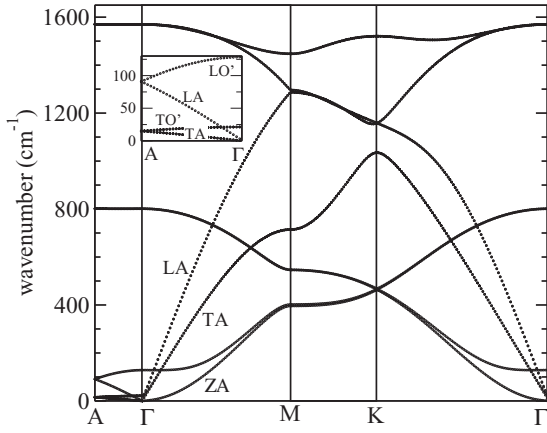
FIG. 2. Phonon dispersion bands of graphite as derived from the LCBOPII potential model in a harmonic approximation. The labels LA, TA, and ZA refer to the acoustic bands employed in the calculation of the elastic stiffness constants. The inset amplifies the low-energy acoustic bands along the Γ-A direction.

bands were obtained by diagonalization of the dynamical matrix along selected symmetry directions in reciprocal space. Interatomic force constants were derived by numerical differentiation of the forces using atom displacements of 1.5×10^{-3} Å with respect to the equilibrium positions. The phonon dispersion in Fig. 2 is similar to that obtained from other empirical potentials and DFT calculations [67]. In Table I we present frequencies of optical modes at the Γ point and acoustic modes at the high-symmetry points M, K, A in k space, derived from DFT calculations in the local-density approximation (LDA) and generalized-gradient approximation (GGA) [67], as well as those obtained with the LCBOPII interatomic potential.

The sound velocities for the three acoustic bands (LA, TA, and ZA) along the direction Γ-M, with wave vectors $(k_x, 0, 0)$, correspond to the slopes $(\partial\omega/\partial k_x)_\Gamma$. For the hexagonal sym-

TABLE I. Phonon frequencies (in cm^{-1}) at high-symmetry points in k space, obtained in Ref. [67] from LDA and GGA-DFT calculations, along with those found for the LCBOPII interatomic potential employed here.

		LDA	GGA	LCBOPII
Γ	LO/TO	1597	1569	1570
	ZO	893	884	901
	TO$'$	43		21
	LO$'$	120		128
M	LA	1346	1338	1266
	TA	626	634	714
	ZA	472	476	396
K	LA/LO	1238	1221	1158
	ZA/ZO	535	539	465
	TA	1002	1004	1035
A	LA/LO$'$	85		90
	TA/TO$'$	30		14

TABLE II. Definition of the six different cell strains employed to calculate the elastic energy and the classical value of the elastic stiffness constants at $T = 0$. The isotropic bulk modulus, B_{iso}, is defined in Eq. (18).

Strain	Components, $e_{ij} \neq 0$	E_{elas}/V_0
1	$e_{xx} = e_{yy} = e$	$(C_{11} + C_{12})e^2$
2	$e_{xx} = -e_{yy} = e$	$(C_{11} - C_{12})e^2$
3	$e_{zz} = e$	$\frac{1}{2}C_{33}e^2$
4	$e_{xz} = e_{zx} = e$	$2C_{44}e^2$
5	$e_{xx} = e_{yy} = e_{zz} = e$	$\frac{9}{2}B_{\text{iso}}e^2$
6	$e_{xx} = e_{yy} = -\frac{e}{3}, \ e_{zz} = \frac{2e}{3}$	$\frac{1}{9}(C_{11} + C_{12} + 2C_{33} - 4C_{13})e^2$

metry of graphite, these velocities are related to the elastic stiffness constants as follows [68]:

$$\omega_{\text{LA}} = \left(\frac{C_{11}}{\rho}\right)^{1/2} k_x, \tag{1}$$

$$\omega_{\text{TA}} = \left(\frac{C_{11} - C_{12}}{2\rho}\right)^{1/2} k_x, \tag{2}$$

$$\omega_{\text{ZA}} = \left(\frac{C_{44}}{\rho}\right)^{1/2} k_x, \tag{3}$$

where ρ is the density of graphite. Along the Γ-A direction, $(0, 0, k_z)$, the sound velocities of the LA and the twofold-degenerate TA branches are given by [68]

$$\omega_{\text{LA}} = \left(\frac{C_{33}}{\rho}\right)^{1/2} k_z, \tag{4}$$

$$\omega_{\text{TA}} = \left(\frac{C_{44}}{\rho}\right)^{1/2} k_z. \tag{5}$$

The interatomic potential LCBOPII was employed earlier to obtain the phonon dispersion bands of graphene [69]. We note that the version of the potential used in that work was slightly different than that employed here, which is more realistic to describe the bending of the graphene sheets [50,52], as mentioned above in Sec. II.

Our second approach to determine C_{ij} at $T = 0$ consists of calculating the elastic energy, E_{elas}, for small strains e_{ij}, which can be expressed as

$$\frac{E_{\text{elas}}}{V_0} = \frac{E - E_0}{V_0} = \frac{1}{2} \sum_{i=1}^{6} \sum_{j=1}^{6} C_{ij} e_i e_j, \tag{6}$$

where E_0 and V_0 are the energy and volume of the equilibrium configuration in the absence of strain (see below). We use the Voigt notation, where the components of the strain tensor are labeled as

$$\{e_i, i = 1, \ldots, 6\} = \{e_{xx}, e_{yy}, e_{zz}, e_{yz}, e_{xz}, e_{xy}\}. \tag{7}$$

The elastic energy corresponding to six different strain tensors, employed in the evaluation of C_{ij}, is summarized in Table II. The tensor components are defined with the help of a dimensionless constant e. The elastic stiffness constants were obtained by quadratic fits of the function E_{elas}/V_0 for strains defined in the region $|e| \leqslant 2 \times 10^{-3}$. One important aspect in the calculation of the elastic energy is that, whenever the solid lattice is subjected to a uniform strain, the atoms will

TABLE III. Elastic stiffness constants, bulk modulus, and Poisson's ratio of graphite, derived from classical and quantum simulations at $T = 0$, 300, and 750 K. Data for C_{ij} and B are in GPa. We give in parentheses the statistical error in the last digit.

	$T = 0$		$T = 300$ K		$T = 750$ K	
	classical	quantum	classical	quantum	classical	quantum
C_{11}	1007.7(5)	992(1)	969(1)	960(2)	917(2)	910(2)
C_{12}	216.3(3)	174(1)	175(1)	162(2)	134(1)	131(2)
C_{13}	1.05(4)	1.0(1)	3.4(1)	3.4(1)	5.7(1)	5.7(1)
C_{33}	37.1(1)	35.9(1)	34.6(1)	33.9(1)	31.6(1)	31.2(1)
C_{44}	1.03(2)	0.74(1)	0.61(1)	0.57(1)	0.42(2)	0.41(2)
B	35.1(1)	33.8(1)	33.0(1)	32.3(1)	30.4(1)	30.0(1)
ν	0.215	0.175	0.181	0.169	0.146	0.144

rearrange themselves in the distorted lattice to minimize the elastic energy [70–72]. This aspect is especially important in the case of strain 2 in Table II, where upon a uniform distortion of the lattice, one finds that the elastic energy is reduced by 13% when internal relaxation of atomic positions in the distorted lattice is allowed. Only when this atomic relaxation is included do the elastic constants calculated by the elastic-energy method and the acoustic phonon dispersion agree with each other [71]. Our results for the classical $T \to 0$ limit of the elastic stiffness constants of graphite are summarized in Table III, along with also finite-temperature values which will be discussed below. The error bars in the classical zero-temperature values were derived from the differences encountered between both methods employed here, except for C_{13}, where the error bar corresponds to the results obtained with strains 5 and 6.

IV. ENERGY

In this section we present the internal energy of unstressed graphite, obtained from PIMD simulations in the isothermal-isobaric ensemble at various temperatures. These kinds of simulations yield separately the kinetic and potential energy of the system [41,73], which allows us to analyze anharmonicities in the solid by comparing both energies. For given temperature and external stress, we express the internal energy as $E = E_0 + E_{pot} + E_{kin}$, where E_{pot} and E_{kin} are the kinetic and potential energy, and E_0 is the energy of the classical model at $T = 0$, i.e., the minimum-energy configuration of the considered LCBOPII potential, with totally planar sheets and no atomic quantum delocalization.

In the classical minimum, the energy of graphite decreases by 50 meV/atom with respect to an isolated graphene monolayer. This stabilization energy, associated with layer interactions, is in line with that found from classical Monte Carlo simulations of bilayer graphene using the LCBOPII potential [54] (25 meV/atom, since in this case each graphene layer has only one neighboring layer). The interlayer binding energies obtained from various *ab initio* calculations for the AB stacking of graphite display a rather large dispersion, with most data between 20 and 80 meV/atom [12,74,75]. Experimental values at room temperature lie between 35 and 52 meV/atom [12].
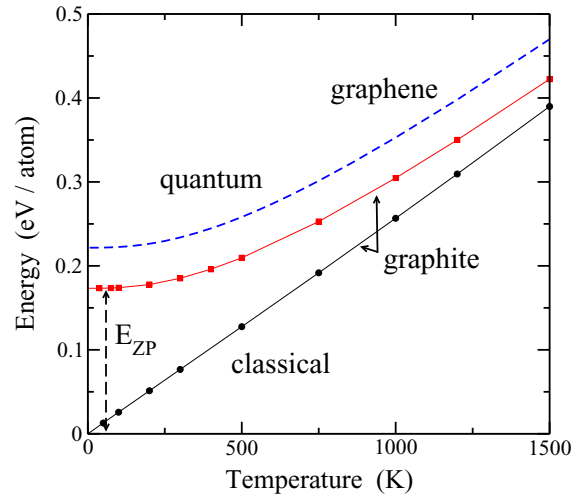

FIG. 3. Internal energy of unstressed graphite as a function of temperature, obtained from PIMD (squares) and classical MD simulations (circles). Solid lines are guides to the eye. Error bars are less than the symbol size. A vertical dashed arrow indicates the zero-point energy, $E_{ZP} = 173$ meV/atom. A dashed line shows the internal energy of monolayer graphene, as derived from PIMD simulations.

In Fig. 3 we display the temperature dependence of the internal energy per atom, $E - E_0$, as derived from our PIMD simulations of unstressed graphite (solid squares). For comparison, we also show the internal energy obtained from classical MD simulations (circles). In the quantum case, $E - E_0$ converges in the low-T limit to a zero-point energy $E_{ZP} = 173$ meV/atom. This value is slightly higher than that corresponding to a graphene monolayer [33] ($E_{ZP} = 171$ meV/atom), which indicates that most of the zero-point energy is due to high-frequency in-plane vibrational modes, which are not appreciably changed by the interaction between layers.

In the quantum model, the internal energy follows at low temperature ($T < 200$ K) a dependence $E - E_0 \sim T^3$, which is consistent with the known dependence $c_p \sim T^2$ for the specific heat of graphite in this temperature region [76,77]. The classical model yields at low T a dependence $E - E_0 \sim T$, as expected from the equipartition principle in classical statistical mechanics for harmonic lattice vibrations, which gives the Dulong-Petit law: $c_p = 3Nk_B$ irrespective of T. At high T we find from the classical simulations slight deviations from this law, due to anharmonicity of the vibrational modes. The energy data found from PIMD simulations converge to those of classical MD simulations as temperature is raised. However at $T = 1000$ K we still observe a significant difference between quantum and classical results, close to 50 meV/atom.

The dashed line in Fig. 3 represents the internal energy per atom for a graphene monolayer, as derived from PIMD simulations. This line is shifted upward by $\Delta E = 48$ meV/atom with respect to the quantum data of graphite, which is the effective interlayer interaction. This value is slightly lower than that found in the classical calculation at $T = 0$ ($\Delta E = 50$ meV/atom), due to the larger zero-point energy per atom in graphite.
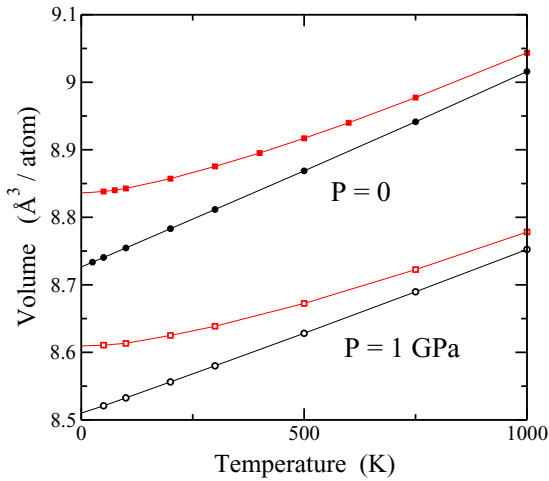
FIG. 4. Temperature dependence of the crystal volume of graphite, as derived from PIMD (squares) and classical MD (circles) simulations for $P = 0$ (solid symbols) and a hydrostatic pressure $P = 1$ GPa (open symbols). Error bars are smaller than the symbol size.

As indicated above, an overall quantification of the anharmonicity of vibrational modes in graphite can be obtained by comparing the kinetic and potential energy yielded by PIMD simulations. For strictly harmonic vibrations, one has $E_{kin} = E_{pot}$ (virial theorem), so departure from pure harmonicity can be assessed in view of deviations from unity of the ratio E_{kin}/E_{pot}. At low T, we find for graphite a ratio $E_{kin}/E_{pot} = 1.02$. From earlier analysis of anharmonicity in solids, on the basis of quasiharmonic approximations and perturbation theory, it is known that for small T, changes in the vibrational energy with respect to a harmonic approach are essentially due to the kinetic-energy contribution. Indeed, for a perturbed harmonic oscillator with an energy perturbation proportional to r^3 or r^4 at $T = 0$ (here r is any coordinate in the problem), the first-order change in the energy is due to a variation of E_{kin}, and E_{pot} remains changeless as in the unperturbed oscillator [78,79].

V. STRUCTURAL VARIABLES

A. Crystal volume

In Fig. 4 we present the volume per atom as a function of temperature, as derived from classical MD (circles) and PIMD simulations (squares) in the NPT ensemble for zero external stress (solid symbols) and a hydrostatic pressure $P = 1$ GPa (open symbols). As is usual in thermodynamics, and in the definition of the bulk modulus considered below, a compressive pressure is positive. In the stress-tensor notation employed in elasticity this corresponds to $\tau_{xx} = \tau_{yy} = \tau_{zz} = -1$ GPa, and $\tau_{\alpha\beta} = 0$ for $\alpha \neq \beta$.

We comment first on the results for the unstressed material. The data derived from classical simulations display a temperature dependence of the volume close to linear, with a positive slope dV/dT slowly increasing for rising T. These data converge at low temperature to $V_0 = 8.727$ Å^3/atom, which corresponds to the minimum-energy volume. For comparison, we mention that earlier theoretical work based mainly

on DFT calculations gave values for V_0 between 8.61 and 8.94 Å^3/atom [10,11,80,81]. The equilibrium volume obtained from PIMD simulations at each temperature is larger than the classical result, and converges to 8.837 Å^3/atom for $T \rightarrow 0$. This represents a zero-point volume expansion of 1.3% with respect to the classical minimum. At high temperature the quantum and classical data converge one to the other. Our results are not far from the volume obtained for graphite at ambient conditions from x-ray diffraction experiments: 8.78 and 8.80 Å^3/atom in Refs. [82] and [83], respectively.

At low temperature ($T \rightarrow 0$) the interlayer distance, c, increases from the classical limit by 0.4%, and the linear expansion in the sheet plane (x and y directions) amounts also to 0.4%. The zero-point expansion of a crystal is controlled by the anharmonicity of the lattice vibrations. In terms of a QHA, this expansion depends on each phonon through the product of its zero-point energy and the corresponding Grüneisen parameter [13,66,84,85]. Given that the main contributions to the in-plane and out-of-plane expansions are dominated by phonons with different polarization, it seems accidental that the relative quantum effects in directions x and z coincide, in spite of the large anisotropy of the material. This anisotropy is, however, clearly observable in the thermal expansion at finite temperatures (see Sec. VI).

For graphite under a hydrostatic pressure $P = 1$ GPa, we obtain classical and quantum results similar to those found for the unstressed material, with the following differences. First, the volume is reduced, but this reduction is much less in the (x, y) plane than in the out-of-plane z direction, which corresponds to the different magnitudes of the elastic constants governing the compressibility in different crystal directions (see below). Second, the zero-point volume expansion is reduced with respect to that found for unstressed graphite. For $P = 1$ GPa we find $\Delta V = 0.099$ Å^3/atom for $T \rightarrow 0$ vs an expansion of 0.110 Å^3/atom for $P = 0$. Third, the thermal dilation decreases under an applied hydrostatic pressure. In the temperature range from $T = 0$ to 1000 K, we find from the PIMD data an expansion of 0.169 and 0.207 Å^3/atom for the stressed and unstressed material, respectively.

The dependence of crystal volume on hydrostatic pressure is displayed in Fig. 5 for several temperatures. Symbols are data points derived from PIMD simulations and solid lines are guides to the eye. The dashed line indicates the pressure dependence of V for the classical model at $T = 0$. For each pressure P, this corresponds to the minimum of the enthalpy $H = E - PV$. Note the important difference between this classical result at $T = 0$ and the quantum result at $T = 100$ K (more than 0.1 Å^3/atom), due to the low-temperature crystal expansion for the quantum model, as shown in Fig. 4. The solid lines in Fig. 5 seem at first sight rather parallel, but differences between their slopes (in particular at $P = 0$) indicate changes in the bulk modulus of the material (see below). The volume differences between these isotherms become smaller as the hydrostatic pressure is increased. Thus, the difference between the quantum result at 100 K and the classical minimum is reduced by 13% from $P = 0$ to 1 GPa.

Volume changes under a hydrostatic pressure are related to the bulk modulus B, as discussed in Sec. VIII. From the classical data at $T = 0$, we have $dV/dP = -0.246$ Å^3/(atom GPa) in the limit $P \rightarrow 0$, whereas at $T = 1000$ K,
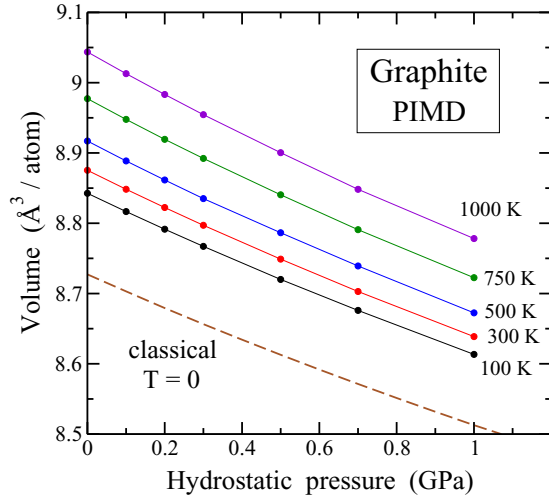
FIG. 5. Volume of graphite as a function of hydrostatic pressure at various temperatures, as derived from PIMD simulations. From top to bottom, $T = 1000, 750, 500, 300,$ and 100 K. Solid lines are guides to the eye. A dashed line represents the pressure dependence of the classical volume at $T = 0$.
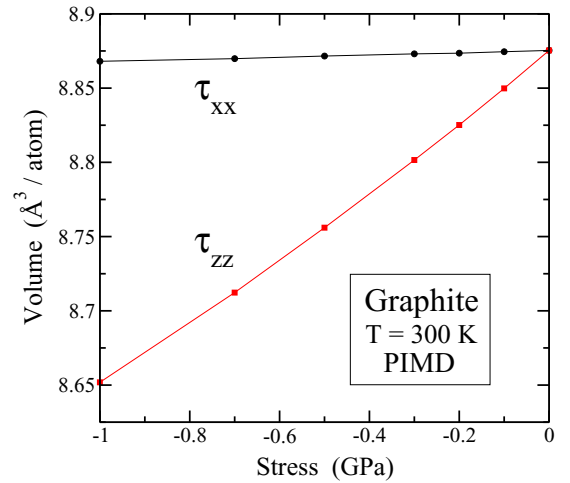

FIG. 6. Volume of graphite as a function of uniaxial stress along the x and z directions of the orthorhombic simulation cell at $T = 300$ K. τ_{xx} and τ_{zz} indicate the nonvanishing components of the stress tensor in each case. Symbols represent results of PIMD simulations, with error bars less than the symbol size. Lines are guides to the eye.

our PIMD simulations yield $dV/dP = -0.313$ Å^3/(atom GPa).

The strain components e_{xx} and e_{zz} for a hydrostatic pressure P can be obtained from the elastic compliance constants S_{ij} as [63,65]

$$\frac{e_{xx}}{e_{zz}} = \frac{S_{11} + S_{12} + S_{13}}{2S_{13} + S_{33}}. \tag{8}$$

At room temperature ($T = 300$ K) we find from our PIMD simulations $e_{xx}/e_{zz} = 0.027$. At 1000 K this ratio decreases to 0.023.

For the calculation of elastic constants at finite temperatures presented in Sec. VII, we have carried out simulations of graphite under various kinds of stress, given by the different components of the tensor $\{\tau_{ij}\}$, as explained in Sec. II. In Fig. 6 we present the dependence of the crystal volume on uniaxial stress along the x and z directions at $T = 300$ K, as derived from PIMD simulations. These uniaxial stresses correspond to nonvanishing components of the stress tensor τ_{xx} and τ_{zz}, respectively. The volume change in the second case is much larger than in the former, due to the higher compressibility in the z direction, perpendicular to the layer planes. For τ_{xx} and τ_{zz} close to zero we find for the stress derivative of the volume values of -7.2×10^{-3} and -0.256 Å^3/(atom GPa), respectively.

The volume change under a uniaxial stress can be obtained from the elastic constants of the material, in particular from the compliance constants. We have [63,65]

$$\frac{\Delta V}{V} = e_{xx} + e_{yy} + e_{zz} = (S_{11} + S_{12} + S_{13})\tau_{xx}, \tag{9}$$

or, for the stress derivative of the volume,

$$\frac{dV}{d\tau_{xx}} = (S_{11} + S_{12} + S_{13})V. \tag{10}$$

Similarly, for a uniaxial stress τ_{zz}, one has

$$\frac{dV}{d\tau_{zz}} = (2S_{13} + S_{33})V. \tag{11}$$

Note that the ratio of these stress derivatives of the volume coincides with the ratio e_{xx}/e_{zz} given above for a hydrostatic pressure.

B. In-plane area

In the graphene literature, researchers have discussed with great detail the behavior of the in-plane area of the 2D material, which in the case of graphite corresponds to the area $L_x L_y$ on the xy plane of the simulation box. Here we will consider the in-plane area per atom, $A_p = L_x L_y/n$. In Fig. 7 we show the temperature dependence of A_p for unstressed graphite, as derived from classical MD (circles) and PIMD simulations (squares). At first sight one observes an important difference between the quantum and classical results. In the quantum data we find a decrease in A_p for rising T until a temperature of about 600 K, for which it reaches a minimum, and an increase in A_p at higher T. In contrast, in the classical data we obtain a rise (roughly linear) of A_p at low T, and an increase faster than linear at $T > 500$ K. At $T = 1500$ K the difference between classical and quantum data for A_p is still much larger than the error bars of the simulation results (smaller than the symbol size in Fig. 7).

In the low-temperature limit ($T \to 0$), the in-plane area A_p derived from PIMD simulations converges to 2.6371 Å^2/atom, with a C-C bond length $d_{\text{C-C}} = 1.4276$ Å. For the classical minimum we find a value $A_0 = 2.6149$ Å^2/atom, which corresponds to a C-C distance $d_0 = 1.4188$ Å. This gives for the quantum result a zero-point expansion in the area A_p of 0.022 Å^2/atom, i.e., a relative increase of about 1%, associated with the rise in C-C bond length. Looking at the C-C distance for the classical minimum, d_0, we observe that there is a slight in-plane lattice contraction with respect to the
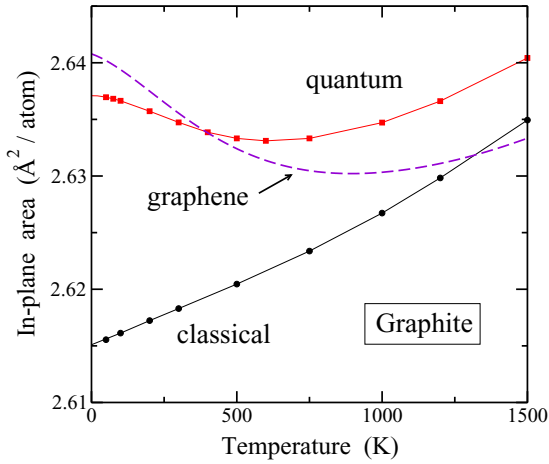
FIG. 7. Temperature dependence of the in-plane area per atom, A_p, obtained from classical (circles) and PIMD (squares) simulations for $n = 240$. Error bars are less than the symbol size. Solid lines are guides to the eye. A dashed line indicates the dependence of A_p on T for a graphene monolayer, as derived from PIMD simulations for the same system size.
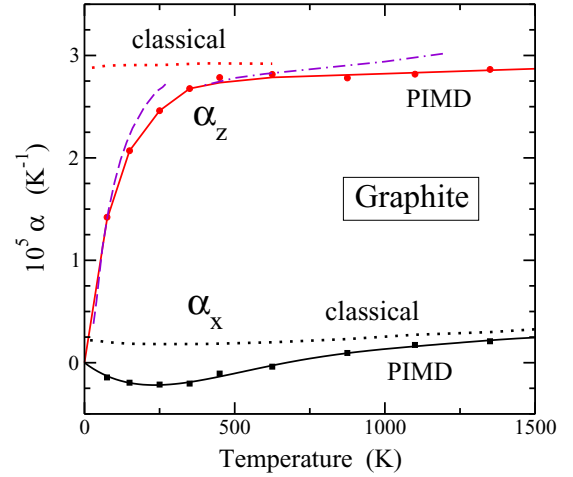

FIG. 8. Linear thermal expansion coefficients of graphite vs temperature: α_x along the in-plane x direction and α_z along the out-of-plane z direction. Symbols represent data obtained from PIMD simulations for $n = 960$ and solid lines are guides to the eye. Dotted lines indicate results derived from classical MD simulations. The dashed line represents data obtained for α_z by Bailey and Yates [88] from interferometric measurements at $T < 300$ K. The dashed-dotted line is a fit to experimental data of α_z for $T > 300$ K [63].

cases of a graphene monolayer ($d_0 = 1.4199$ Å) and bilayer ($d_0 = 1.4193$ Å), as a consequence of interlayer interactions [33,39]. We note that although in the classical model one has planar carbon sheets for $T \to 0$, in the quantum zero-temperature limit the layers are not exactly planar, since there is an atomic zero-point motion in the out-of-plane z direction [33,48].

For comparison with the results for graphite, we also present in Fig. 7 the area A_p obtained from PIMD simulations of monolayer graphene with the same size $n = 240$ (dashed line). In this case, the shape of the temperature dependence is similar to that of graphite, with a decrease in A_p at low T and an increase at high T. For graphene, however, the decrease is larger and the minimum of A_p occurs at a higher temperature. At low T, the area A_p of graphite is reduced by 4×10^{-3} Å^2/atom with respect to a graphene monolayer, as a consequence of layer interactions.

The fact that $dA_p/dT < 0$ at low temperature, as obtained in the quantum simulations, is due to the out-of-plane motion of the carbon atoms, which dominates over the thermal expansion of the C-C bonds in the graphite layers. This effect is not captured by a classical model for the atomic motion, as happens in classical MD simulations, where the relative contributions of the different vibrational modes are not correctly represented at low temperatures. At high T, the bond expansion dominates over the contraction associated with motion in the z direction, so that $dA_p/dT > 0$ in both classical and quantum models.

VI. THERMAL EXPANSION

At low T our PIMD simulations give for graphite with AB stacking an interlayer spacing $c = 3.3510$ Å. For the classical model at $T = 0$ (minimum energy configuration with planar graphene sheets) we find $c_0 = 3.3372$ Å. Thus, we have a zero-point expansion $\Delta c = 1.4 \times 10^{-2}$ Å. At $T = 300$ K, we

have $c = 3.3688$ Å from PIMD simulations, not far from a distance of 3.3538 Å obtained by Baskin and Meyer from x-ray diffraction measurements at room temperature ($T = 297$ K) [86]. At 300 K, the difference between quantum and classical results is around four times smaller than for the low-temperature limit.

From the mean interlayer spacing we consider the linear thermal expansion coefficient (TEC) α_z, defined as

$$\alpha_z = \frac{1}{c}\left(\frac{\partial c}{\partial T}\right)_\tau. \qquad (12)$$

This TEC for vanishing external stress has been commonly denoted as α_c in the literature, but we will call it here α_z for notation consistency. Data for α_z obtained from PIMD simulations of graphite are presented in Fig. 8 as solid circles. These data points were obtained from a numerical derivative of the mean layer spacing c found in the simulations at several temperatures. One observes a fast rise of α_z in the low-temperature region up to around 200 K, and at higher T this rise becomes much slower. At 300 K we find $\alpha_z = 2.6 \times 10^{-5}$ K^{-1}. For comparison, we also present in Fig. 8 results of classical MD simulations for α_z (dotted line). They converge at low T to a value $\alpha_z = 2.9 \times 10^{-5}$ K^{-1}. Note the inconsistency of this classical result with the third law of thermodynamics, which requires that TECs should vanish for $T \to 0$ [66,87].

Experimental data for α_z of pyrolytic graphite at low T were obtained by Bailey and Yates [88] from interferometric measurements (dashed line in Fig. 8). The dashed-dotted line indicates a fit to experimental data from several sources at $T > 300$ K, presented by Marsden *et al.* [63]. Both dashed and dashed-dotted lines derived from experimental data do not fit well one with the other close to room temperature, due to the dispersion of data in different source references.

At $T > 500$ K we observe that the TEC α_z obtained from our PIMD simulations rises slower than the line fitted to experimental data in Ref. [63].

In the xy layer plane, we consider a linear TEC defined as

$$\alpha_x = \frac{1}{L_x}\left(\frac{\partial L_x}{\partial T}\right)_\tau. \qquad (13)$$

In Fig. 8 (bottom) we display α_x obtained from PIMD simulations of graphite up to 1500 K (solid squares). The solid line represents a polynomial fit to the data points. At low temperature this TEC is negative and reaches a minimum at $T_m \approx 250$ K. For $T > T_m$, α_x increases for rising temperature and becomes positive at $T_m \approx 600$ K, which coincides with the temperature at which the in-plane area A_p attains its minimum value, as shown in Fig. 7. For comparison, the dotted line in Fig. 8 (bottom) represents the results obtained for α_x from classical MD simulations. This classical α_x takes positive values in the whole temperature region considered here, and converges at low T to a (nonphysical) value of 2.2×10^{-6} K^{-1}. The quantum data for α_x are below the classical ones, and for $T > 1500$ K they are close one to the other.

Our results for α_x show a temperature dependence similar to those obtained earlier employing other theoretical techniques, in particular that found by Mounet and Marzari [13] from a combination of DFT calculations with a QHA for the vibrational modes. These authors found for α_x a minimum of -1.2×10^{-6} K^{-1} for $T \approx 250$ K and a vanishing TEC for $T \approx 500$ K. Experimental results for the TEC α_x show a minimum at a temperature between 200 and 300 K, similarly to the data obtained from our quantum simulations [63,89,90]. Several experimental data sets display a minimum of about -1.5×10^{-6} K^{-1}, which turns out to be somewhat less than our data presented in Fig. 8.

VII. LINEAR ELASTIC CONSTANTS AT FINITE TEMPERATURES

In this section we present and discuss nuclear quantum effects in the elastic stiffness constants of graphite. Such effects are present in general for the different elastic constants, mainly at low temperature, but they turn out to be especially large for C_{12} and C_{44}. In Fig. 9(a) we present the temperature dependence of the elastic constant C_{12}, as derived from our classical (circles) and PIMD (squares) simulations. The classical finite-temperature results converge at low T to the value obtained from the phonon dispersion, indicated by an open circle in Fig. 9(a). In the limit $T \to 0$, this elastic constant is found to decrease from the classical value of 216 GPa to 174 GPa due to zero-point motion. This represents a reduction of 19% with respect to the classical result. At room temperature the quantum reduction amounts to a 7%.

In Fig. 9(b) we display the dependence of C_{44} on temperature for both quantum (squares) and classical (circles) cases. The open circle at $T = 0$ represents the value calculated from the phonon dispersion curves as explained in Sec. III [$C_{44} = 1.03(2)$ GPa]. The quantum results converge at low T to $C_{44} = 0.74$ GPa. This elastic constant is particularly interesting from the viewpoint of quantum effects. Given its small value in comparison to other stiffness constants of graphite, at low temperature the quantum correction with respect to the
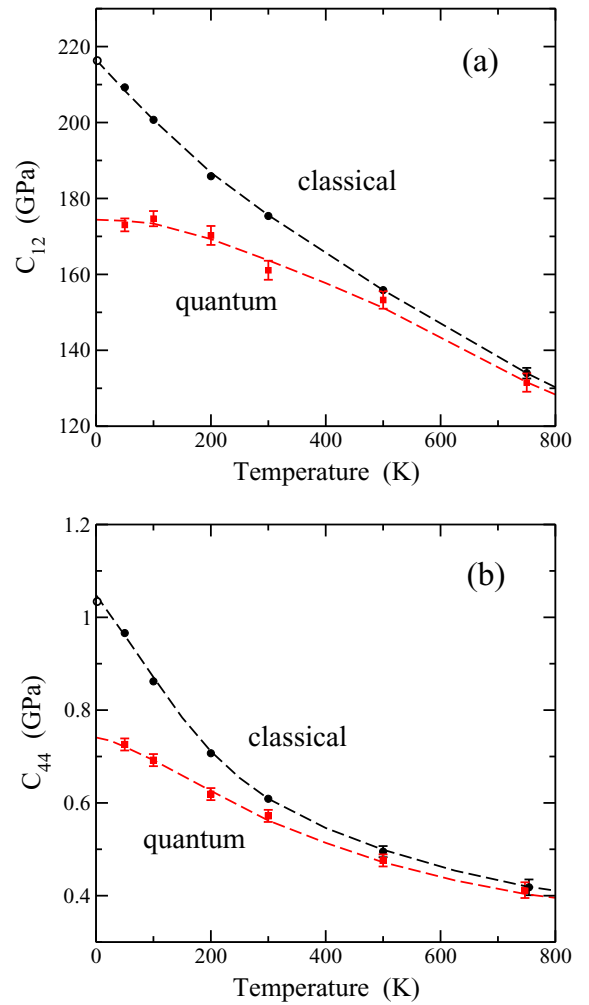

FIG. 9. Temperature dependence of the elastic constants: (a) C_{12} and (b) C_{44}, as derived from classical MD (circles) and PIMD (squares) simulations in the NVT ensemble. Open circles in (a) and (b) represent the classical value at $T = 0$, calculated from the phonon dispersion curves. Error bars, when not shown, are in the order of the symbol size. Lines are guides to the eye.

classical result is very large. In the limit $T \to 0$, it means a relative reduction of C_{44} by 28%.

Concerning nuclear quantum effects, something similar occurs for other elastic stiffness constants, as C_{11} and C_{33}, for which results of classical and PIMD simulations are given in Table III at $T = 300$ and 750 K, as well as for the low-T limit. In all cases, the classical value at $T = 0$ is calculated from the phonon dispersion bands and lattice strains, as explained in Sec. III. The low-temperature quantum values are obtained from an extrapolation of finite-temperature PIMD results. For C_{11} and C_{33}, zero-point motion causes a decrease of 1.5% and 3.0% with respect to the classical value, respectively. We do not clearly observe any quantum effect in C_{13}. In fact, for this stiffness constant the results of PIMD and classical MD simulations coincide within error bars in the temperature region considered here.

It is worthwhile commenting on the relation between the temperature dependence of the linear elastic constants shown in Fig. 9 and the quantum delocalization of atomic nuclei.

TABLE IV. Elastic stiffness constants, bulk modulus B, and Poisson's ratio ν of graphite obtained from various experimental techniques by different authors at ambient conditions. Data for C_{ij} and B are given in GPa. The bulk modulus B is obtained in each case from the elastic constants by using Eq. (16).

	Blakslee [7]	Bosak [8]	Nicklow [9]
C_{11}	1060(20)	1109(16)	1440(200)
C_{12}	180(20)	139(36)	
C_{13}	15(5)	0(3)	
C_{33}	36.5(1)	38.7(7)	37.1(5)
C_{44}	0.27(9)	5.0(3)	4.6(2)
B	35.8(2)	36.4(11)	
ν	0.17	0.13	

For C_{12} and C_{44}, we find in the classical results a decrease as temperature is raised. This is related to classical thermal motion of the carbon atoms, which grows with temperature as indicated by the MSD shown in Fig. 1. In the results of our quantum PIMD simulations we observe an important decrease in the zero-temperature elastic constants, due to zero-point delocalization (finite MSD), with respect to the classical values, where the atomic MSD vanishes. As temperatures increases, the quantum and classical results converge one to the other, as happens for the MSD. Something similar can be said for the results of the bulk modulus presented below in Sec. VIII.

In Table IV we present values of the elastic stiffness constants derived from experimental data by several authors, from a combination of ultrasonic, sonic resonance, and static test methods [7], as well as inelastic x-ray scattering [8] and inelastic neutron scattering along with a force model [9]. There appears some dispersion in these results derived from experiments at ambient conditions, in particular for C_{13} and C_{44}, as can be seen in our Table IV and in Refs. [7,8]. For C_{44} these values range from 5.0 GPa to less than 1 GPa. The low value $C_{44} = 0.27(9)$ GPa obtained by Blakslee *et al.* [7] may be due to the presence of dislocations in the studied material, as suggested by the authors. In a later paper, Seldin and Nezbeda [91] found that this elastic constant rises when the graphite samples are irradiated with neutrons at several temperatures. These authors found that natural graphite crystals have after irradiation a shear modulus C_{44} in the range 1.6–4.6 GPa. Experimental data for C_{13} of graphite are scarce, and different techniques have yielded diverse outcomes. The results found

by Bosak *et al.* [8] were compatible with a vanishing C_{13} (within their error bars).

In Table V we give values of the elastic constants of graphite calculated by various research groups. Several calculations were carried out in the framework of DFT, with both local-density approximation (LDA) and generalized-gradient approximation (GGA) [10,12,13]. Moreover, Jansen and Freeman [11] employed the full-potential linearized augmented-plane wave (FLAPW) method, and Michel and Verberck obtained the elastic constants from the phonon spectrum calculated with an effective potential [14]. In spite of the general reliability of these theoretical procedures, there are some discrepancies between the results of the different research groups. A common feature of the data derived from DFT calculations is that they yielded $C_{13} < 0$, as shown in Table V. Although this is not forbidden for the stability of hexagonal crystals [92], we are not aware of any experimental work on graphite where C_{13} was found to be negative. We also note the anomalous (very small) value obtained for C_{33} in Ref. [12] from DFT-GGA calculations, which seems to be due to a largely underestimated interlayer interaction. Our main conclusion concerning the linear elastic constants of graphite is that the intrinsic difficulty of calculating the elastic constants of this largely anisotropic material is still more complicated at temperatures lower than the Debye temperature of the material, where nuclear quantum effects are relevant.

From the elastic stiffness constants one can obtain the Poisson's ratio ν, which is a measure of the relation between the transverse and longitudinal strains under an applied stress. For graphite one has $\nu = C_{12}/C_{11}$. In Table III we give the Poisson's ratio calculated from the elastic constants yielded by our classical and quantum simulations. In our results, ν is found to decrease as temperature is raised. In the low-temperature limit, nuclear quantum motion causes a reduction of ν from 0.215 to 0.175; i.e., it decreases by 19%. At $T = 300$ K the classical and quantum values are 0.181 and 0.169, respectively, with a decrease of 7% due to quantum motion. At 750 K this decrease is small, about 1%.

In Table IV we give values of the Poisson's ratio obtained from the elastic constants found in experimental works [7,8]. The value derived from the work of Blakslee *et al.* [7] is close to our quantum result at $T = 300$ K, and that from the paper by Bosak *et al.* [8] is somewhat lower. Data derived from theoretical methods given in Table V are close to our classical value at $T = 0$, $\nu = 0.215$. A larger collection of

TABLE V. Elastic stiffness constants, bulk modulus, and Poisson's ratio of graphite obtained from various calculations based on density-functional theory with LDA and GGA, as well as FLAPW and lattice dynamics (Latt. dyn.). Values indicated with an asterisk (*) correspond to $C_{11} + C_{12}$. Data for C_{ij} and B are given in GPa. The bulk modulus B is obtained in each case from the elastic constants by means of Eq. (16).

	LDA [10]	FLAPW [11]	LDA, GGA [12]	LDA, GGA [13]	Latt. dyn. [14]
C_{11}	1279.6*	1430*		1118, 1079	1211.3
C_{12}				235, 217	275.5
C_{13}	−0.5	−12		−2.8, −0.5	0.59
C_{33}	40.8	56	30.4, 0.8	29.5, 42.2	36.79
C_{44}				4.5, 3.9	4.18
B	38.3	50.2		28.0, 39.6	35.1
ν				0.210, 0.201	0.227

data for the Poisson's ratio of graphite derived from theoretical methods is given in Ref. [93]. The data reported in the literature display a large dispersion, most of them lying in the region from 0.12 to 0.3. We note that the Poisson's ratio usually considered for graphite is an in-plane variable; i.e., it refers to the x and y directions. One can equally define an out-of-plane ratio ν_{xz}, referring to the x and z directions. In this case, $\nu_{xz} = C_{13}/C_{11}$, and we find from our PIMD simulations at 300 K $\nu_{xz} = 3.5 \times 10^{-3}$.

VIII. BULK MODULUS

We present here results for the isothermal bulk modulus, $B = -V(\partial P/\partial V)_T$, derived from our classical MD and quantum PIMD simulations. To check the overall consistency of our procedures, we obtain B in three different ways: (1) calculating $\partial P/\partial V$ from a numerical differentiation for positive and negative hydrostatic pressures P close to $P = 0$, (2) from the volume fluctuations along NPT simulation runs at temperature T, and (3) from the elastic constants obtained from the simulations.

In the isothermal-isobaric ensemble (our second method), the bulk modulus can be directly calculated from the mean-square fluctuations of the volume, σ_V^2, using the formula [94,95]

$$B = \frac{k_B T V}{\sigma_V^2}, \qquad (14)$$

k_B being Boltzmann's constant. This expression has been employed earlier to obtain the bulk modulus of various kinds of solids from path-integral simulations [34,95].

The bulk modulus of graphite can also be calculated from the elastic constants of the material (our third procedure). For a hydrostatic pressure P, we have $\tau_{xx} = \tau_{yy} = \tau_{zz} = -P$, so that

$$\frac{\Delta V}{V} = e_{xx} + e_{yy} + e_{zz} = -(2S_{11} + 2S_{12} + 4S_{13} + S_{33})P, \qquad (15)$$

and using the relations between stiffness and compliance constants [63,65], we find

$$B = -V\frac{\partial P}{\partial V} = \frac{(C_{11} + C_{12})C_{33} - 2C_{13}^2}{C_{11} + C_{12} + 2C_{33} - 4C_{13}}, \qquad (16)$$

as in Refs. [10,11].

The temperature dependence of the bulk modulus B of graphite derived from our simulations is shown in Fig. 10. Solid and open symbols represent results of classical and quantum simulations, respectively. In each case, symbols represent data obtained from (1) numerical derivative dP/dV (squares), (2) fluctuation formula (circles), and (3) elastic constants (diamonds). The values obtained for the bulk modulus from the three methods agree well in the whole temperature range considered here, for both quantum and classical data. In the limit $T \to 0$, we find $B = 35.1$ and 33.8 GPa for the classical and quantum models, respectively. This means a reduction of the bulk modulus by 4% due to zero-point motion of the C atoms.

In Table III we give values of the bulk modulus B of graphite calculated using Eq. (16) from the stiffness constants derived from our classical and quantum simulations at $T =$
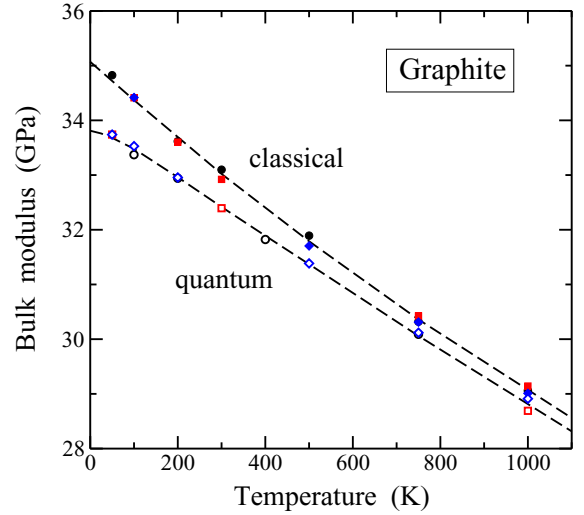

FIG. 10. Temperature dependence of the bulk modulus of graphite, obtained from PIMD (open symbols) and classical MD simulations (solid symbols). The data shown in both cases were obtained by following three different procedures: (1) numerical derivative dP/dV from various hydrostatic pressures P (squares), (2) fluctuation formula in Eq. (14) (circles), and (3) from the elastic constants using Eq. (16) (diamonds). Error bars are on the order of the symbol size. Dashed lines are guides to the eye.

300 and 750 K, as well as for the zero-temperature limit. Values of B obtained from the elastic constants yielded by experimental and theoretical methods are given in Tables IV and V, respectively. From an analysis of the equation of state of graphite at room temperature, Hanfland *et al.* [82] found at ambient pressure $B = 33.8(30)$ GPa, a little higher than our quantum result at 300 K ($B = 32.3$ GPa). Zhao and Spain [83] obtained a somewhat larger value, $B = 35.8(16)$, from x-ray diffraction experiments. Tohei *et al.* [96] found $B = 28.7$ GPa at 300 K from LDA-DFT calculations combined with a QHA for the lattice modes.

One can also define an "isotropic bulk modulus" B_{iso} for isotropic changes of the volume [11], which means $e_{xx} = e_{yy} = e_{zz} = e$ and $\Delta V/V = 3e$. One thus has a hydrostatic pressure

$$P = -\frac{1}{3}(\tau_{xx} + \tau_{yy} + \tau_{zz}), \qquad (17)$$

which gives

$$B_{\text{iso}} = -V\frac{\partial P}{\partial V} = \frac{1}{9}(2C_{11} + 2C_{12} + 4C_{13} + C_{33}). \qquad (18)$$

For the classical limit at $T = 0$ we have $B_{\text{iso}} = 276.6$ GPa, and from our PIMD simulations we find, for $T \to 0$, $B_{\text{iso}} = 263.5$ GPa. At $T = 300$ K, the classical and quantum simulations yield 259.6 and 254.6 GPa, respectively.

IX. SUMMARY

PIMD simulations allow us to quantify nuclear quantum effects in structural and elastic properties in condensed matter. For graphite, in particular, we have seen that such quantum effects are appreciable for T in the order of 500 K, and even

higher for some variables. At low temperature, the quantum zero-point expansion of the graphite volume is non-negligible, and amounts to 1.3% of the classical value. In spite of the large anisotropy of graphite, we have found that the expansion due to zero-point motion is nearly isotropic; i.e., the relative increases in in-plane and out-of-plane directions are approximately the same.

The thermal contraction of the in-plane area ($\alpha_x < 0$) observed in x-ray diffraction experiments at low temperature is reproduced by our quantum simulations, contrary to classical MD, where a positive in-plane thermal expansion is found in the whole temperature range studied here. Given that a negative α_x in layered materials is caused by out-of-plane atomic motion, the in-plane contraction of graphite is essentially due to quantum motion of the C atoms in the z direction. Also, the characteristic trend of α_x (negative at low T and positive at high T) is a clear signature of anharmonicity in the vibrational modes, indicating a coupling between in-plane and out-of-plane modes.

Quantization of lattice vibrations gives rise to changes in the elastic properties of graphite with respect to a classical model. At low temperature, the most significant relative changes in the elastic stiffness constants correspond to C_{12} and C_{44}, where quantum corrections cause a reduction of 19% and 28%, respectively. The bulk modulus and Poisson's ratio decrease by 4% and 19% at low T because of zero-point motion of the carbon atoms. In general, our results indicate that graphite is "softer" than predicted by classical simulations.

In connection with C_{13}, the question is still open as to why several *ab initio* calculations have yielded negative values, which has not been observed in experimental studies. We found here positive values for this elastic constant, but we did not observe any quantum effect on it. All this could be due to a lack of precision in the description of interlayer van-der-Waals-like interactions.

We finally note the consistency of the simulation results with the third law of thermodynamics. This means, in particular, that for $T \rightarrow 0$, thermal expansion coefficients should vanish. Moreover, the temperature derivatives of the elastic stiffness constants and bulk modulus should also vanish.

ACKNOWLEDGMENT

[1] J. Hone, in *Carbon Nanotubes: Synthesis, Structure, Properties, and Applications*, edited by M. S. Dresselhaus, G. Dresselhaus, and P. H. Avouris (Springer, Berlin, 2001), Vol. 80 of Topics in Applied Physics, pp. 273–286.

[2] J. Hone, B. Batlogg, Z. Benes, A. T. Johnson, and J. E. Fischer, Science **289**, 1730 (2000).

[3] A. K. Geim and K. S. Novoselov, Nat. Mater. **6**, 183 (2007).

[4] M. I. Katsnelson, Mater. Today **10**, 20 (2007).

[5] R. Frisenda, Y. Niu, P. Gant, M. Muñoz, and A. Castellanos-Gomez, npj 2D Mater. Appl. **4**, 38 (2020).

[6] P. Ajayan, P. Kim, and K. Banerjee, Phys. Today **69**(9), 38 (2016).

[7] O. L. Blakslee, D. G. Proctor, E. J. Seldin, G. B. Spence, and T. Weng, J. Appl. Phys. **41**, 3373 (1970).

[8] A. Bosak, M. Krisch, M. Mohr, J. Maultzsch, and C. Thomsen, Phys. Rev. B **75**, 153408 (2007).

[9] R. Nicklow, N. Wakabayashi, and H. G. Smith, Phys. Rev. B **5**, 4951 (1972).

[10] J. C. Boettger, Phys. Rev. B **55**, 11202 (1997).

[11] H. J. F. Jansen and A. J. Freeman, Phys. Rev. B **35**, 8207 (1987).

[12] M. Hasegawa and K. Nishidate, Phys. Rev. B **70**, 205431 (2004).

[13] N. Mounet and N. Marzari, Phys. Rev. B **71**, 205214 (2005).

[14] K. H. Michel and B. Verberck, Phys. Rev. B **78**, 085424 (2008).

[15] G. Savini, Y. J. Dappe, S. Oberg, J.-C. Charlier, M. I. Katsnelson, and A. Fasolino, Carbon **49**, 62 (2011).

[16] E. Rollings, G. H. Gweon, S. Y. Zhou, B. S. Mun, J. L. McChesney, B. S. Hussain, A. Fedorov, P. N. First, W. A. de Heer, and A. Lanzara, J. Phys. Chem. Solids **67**, 2172 (2006).

[17] S. Y. Zhou, G. H. Gweon, C. D. Spataru, J. Graf, D. H. Lee, S. G. Louie, and A. Lanzara, Phys. Rev. B **71**, 161403(R) (2005).

[18] C. Kittel, *Introduction to Solid State Physics* (Wiley, New York, 1996), 7th ed.

[19] C. Sevik, Phys. Rev. B **89**, 035422 (2014).

[20] S. Mann, R. Kumar, and V. K. Jindal, RSC Adv. **7**, 22378 (2017).

[21] L. M. Ghiringhelli, J. H. Los, E. J. Meijer, A. Fasolino, and D. Frenkel, Phys. Rev. Lett. **94**, 145701 (2005).

[22] J.-L. Tsai and J.-F. Tu, Mater. Design **31**, 194 (2010).

[23] F. Colonna, A. Fasolino, and E. J. Meijer, Carbon **49**, 364 (2011).

[24] T. Trevethan and M. I. Heggie, Comput. Mater. Sci. **113**, 60 (2016).

[25] A. Petersen and V. Gillette, J. Nucl. Mater. **503**, 157 (2018).

[26] T. Korkut, Ann. Nucl. Energy **63**, 100 (2014).

[27] A. R. Dunn and D. M. Duffy, J. Appl. Phys. **110**, 104307 (2011).

[28] J. Krumhansl and H. Brooks, J. Chem. Phys. **21**, 1663 (1953).

[29] T. Nihira and T. Iwata, Phys. Rev. B **68**, 134305 (2003).

[30] M. J. Gillan, Philos. Mag. A **58**, 257 (1988).

[31] D. M. Ceperley, Rev. Mod. Phys. **67**, 279 (1995).

[32] B. G. A. Brito, L. Cândido, G.-Q. Hai, and F. M. Peeters, Phys. Rev. B **92**, 195416 (2015).

[33] C. P. Herrero and R. Ramírez, J. Chem. Phys. **145**, 224701 (2016).

[34] C. P. Herrero and R. Ramírez, Phys. Rev. B **63**, 024103 (2000).

[35] B. G. A. Brito, G. Q. Hai, and L. Candido, Comput. Mater. Sci. **173**, 109387 (2020).

[36] J. C. Noya, C. P. Herrero, and R. Ramírez, Phys. Rev. B **53**, 9869 (1996).

[37] F. Calvo and Y. Magnin, Eur. Phys. J. B **89**, 56 (2016).

[38] B. G. A. Brito, L. C. DaSilva, G.-Q. Hai, and L. Candido, Phys. Status Solidi B **256**, 1900164 (2019).

[39] C. P. Herrero and R. Ramírez, J. Chem. Phys. **150**, 204707 (2019).

[40] R. P. Feynman, *Statistical Mechanics* (Addison-Wesley, New York, 1972).

[41] C. P. Herrero and R. Ramírez, J. Phys.: Condens. Matter **26**, 233201 (2014).

[42] C. Cazorla and J. Boronat, Rev. Mod. Phys. **89**, 035003 (2017).

[43] J. H. Los, L. M. Ghiringhelli, E. J. Meijer, and A. Fasolino, Phys. Rev. B **72**, 214102 (2005).

[44] A. Fasolino, J. H. Los, and M. I. Katsnelson, Nat. Mater. **6**, 858 (2007).

[45] J. H. Los, A. Fasolino, and M. I. Katsnelson, Phys. Rev. Lett. **116**, 015901 (2016).

[46] K. V. Zakharchenko, M. I. Katsnelson, and A. Fasolino, Phys. Rev. Lett. **102**, 046808 (2009).

[47] A. Politano, A. R. Marino, D. Campi, D. Farías, R. Miranda, and G. Chiarello, Carbon **50**, 4903 (2012).

[48] R. Ramírez and C. P. Herrero, Phys. Rev. B **95**, 045423 (2017).

[49] C. P. Herrero and R. Ramírez, J. Chem. Phys. **148**, 102302 (2018).

[50] R. Ramírez, E. Chacón, and C. P. Herrero, Phys. Rev. B **93**, 235419 (2016).

[51] P. Lambin, Appl. Sci. **4**, 282 (2014).

[52] D. Tisi, Master's thesis, Temperature dependence of phonons in graphene, Università di Modena e Reggio Emilia, Italy, 2017.

[53] L. Spanu, S. Sorella, and G. Galli, Phys. Rev. Lett. **103**, 196401 (2009).

[54] K. V. Zakharchenko, J. H. Los, M. I. Katsnelson, and A. Fasolino, Phys. Rev. B **81**, 235439 (2010).

[55] M. E. Tuckerman, B. J. Berne, and G. J. Martyna, J. Chem. Phys. **97**, 1990 (1992).

[56] M. E. Tuckerman and A. Hughes, in *Classical and Quantum Dynamics in Condensed Phase Simulations*, edited by B. J. Berne, G. Ciccotti, and D. F. Coker (World Scientific, Singapore, 1998), p. 311.

[57] G. J. Martyna, A. Hughes, and M. E. Tuckerman, J. Chem. Phys. **110**, 3275 (1999).

[58] M. E. Tuckerman, *Statistical Mechanics: Theory and Molecular Simulation* (Oxford University Press, Oxford, 2010).

[59] G. J. Martyna, M. E. Tuckerman, D. J. Tobias, and M. L. Klein, Mol. Phys. **87**, 1117 (1996).

[60] C. P. Herrero, R. Ramírez, and E. R. Hernández, Phys. Rev. B **73**, 245211 (2006).

[61] C. P. Herrero and R. Ramírez, J. Chem. Phys. **134**, 094510 (2011).

[62] R. Ramírez, N. Neuerburg, M. V. Fernández-Serra, and C. P. Herrero, J. Chem. Phys. **137**, 044502 (2012).

[63] B. Marsden, A. Mummery, and P. Mummery, Proc. R. Soc. A **474**, 20180075 (2018).

[64] Y. Li and R. B. Thompson, J. App. Phys. **67**, 2663 (1990).

[65] M. Rabiei, A. Palevicius, A. Dashti, S. Nasiri, A. Monshi, A. Vilkauskas, and G. Janusas, Materials **13**, 4380 (2020).

[66] N. W. Ashcroft and N. D. Mermin, *Solid State Physics* (Saunders College, Philadelphia, 1976).

[67] L. Wirtz and A. Rubio, Solid State Commun. **131**, 141 (2004).

[68] R. E. Newnham, *Properties of Materials: Anisotropy, Symmetry, Structure* (Oxford University Press, Oxford, 2005).

[69] L. J. Karssemeijer and A. Fasolino, Surf. Sci. **605**, 1611 (2011).

[70] R. P. Feynman, R. B. Leighton, and M. Sands, *The Feynman Lectures on Physics*, Vol. II (Addison-Wesley, Massachusetts, 1977).

[71] R. Stadler, W. Wolf, R. Podloucky, G. Kresse, J. Furthmüller, and J. Hafner, Phys. Rev. B **54**, 1729 (1996).

[72] J. Zhou and R. Huang, J. Mech. Phys. Solids **56**, 1609 (2008).

[73] R. Ramírez and C. P. Herrero, Phys. Rev. B **84**, 064130 (2011).

[74] M. Hasegawa, K. Nishidate, and H. Iyetomi, Phys. Rev. B **76**, 115424 (2007).

[75] E. Mostaani, N. D. Drummond, and V. I. Fal'ko, Phys. Rev. Lett. **115**, 115501 (2015).

[76] W. Desorbo and G. E. Nichols, J. Phys. Chem. Solids **6**, 352 (1958).

[77] C. P. Herrero and R. Ramírez, Phys. Rev. B **101**, 035405 (2020).

[78] C. P. Herrero and R. Ramírez, Phys. Rev. B **51**, 16761 (1995).

[79] L. D. Landau and E. M. Lifshitz, *Quantum Mechanics* (Pergamon, Oxford, 1965), 2nd ed.

[80] M. C. Schabel and J. L. Martins, Phys. Rev. B **46**, 7185 (1992).

[81] J. Furthmuller, J. Hafner, and G. Kresse, Phys. Rev. B **50**, 15606 (1994).

[82] M. Hanfland, H. Beister, and K. Syassen, Phys. Rev. B **39**, 12598 (1989).

[83] Y. X. Zhao and I. L. Spain, Phys. Rev. B **40**, 993 (1989).

[84] A. Debernardi and M. Cardona, Phys. Rev. B **54**, 11305 (1996).

[85] C. P. Herrero and R. Ramírez, Eur. Phys. J. B **93**, 146 (2020).

[86] Y. Baskin and L. Meyer, Phys. Rev. **100**, 544 (1955).

[87] H. B. Callen, *Thermodynamics* (John Wiley, New York, 1960).

[88] A. C. Bailey and B. Yates, J. Appl. Phys. **41**, 5088 (1970).

[89] E. A. Kellett and B. P. Richards, J. Nucl. Mater. **12**, 184 (1964).

[90] W. C. Morgan, Carbon **10**, 73 (1972).

[91] E. J. Seldin and C. W. Nezbeda, J. Appl. Phys. **41**, 3389 (1970).

[92] F. Mouhat and F.-X. Coudert, Phys. Rev. B **90**, 224104 (2014).

[93] A. Politano and G. Chiarello, Nano Res. **8**, 1847 (2015).

[94] L. D. Landau and E. M. Lifshitz, *Statistical Physics* (Pergamon, Oxford, 1980), 3rd ed.

[95] C. P. Herrero, J. Phys.: Condens. Matter **20**, 295230 (2008).

[96] T. Tohei, A. Kuwabara, F. Oba, and I. Tanaka, Phys. Rev. B **73**, 064304 (2006).